

Development and Test of 2.5-Dimensional Electromagnetic PIC Simulation Code

Sang-Yun Lee¹, Ensang Lee^{1†}, Khan-Hyuk Kim¹, Jongho Seon¹, Dong-Hun Lee¹, Kwang-Sun Ryu²

¹School of Space Research and Institute of Natural Sciences, Kyung Hee University, Yongin 446-701, Korea

²Satellite Technology Research Center, Korea Advanced Institute of Science and Technology, Daejeon 305-701, Korea

We have developed a 2.5-dimensional electromagnetic particle simulation code using the particle-in-cell (PIC) method to investigate electromagnetic phenomena that occur in space plasmas. Our code is based on the leap-frog method and the centered difference method for integration and differentiation of the governing equations. We adopted the relativistic Buneman-Boris method to solve the Lorentz force equation and the Esirkepov method to calculate the current density while maintaining charge conservation. Using the developed code, we performed test simulations for electron two-stream instability and electron temperature anisotropy induced instability with the same initial parameters as used in previously reported studies. The test simulation results are almost identical with those of the previous papers.

Keywords: particle simulation, PIC method, two-stream instability, whistler instability

1. INTRODUCTION

The Particle-In-Cell (PIC) method is a technique commonly used to simulate the dynamics of charged particles interacting with electromagnetic fields. Since the 1950s, the PIC method has been used for self-consistent kinetic simulations along with the Vlasov simulation method. The PIC method is useful to study the dynamics of plasmas that takes place on spatial and temporal scales that magnetohydrodynamics (MHD) cannot handle properly.

In this paper, we present the development of a 2.5-dimensional relativistic electromagnetic PIC code. The code is developed to study electromagnetic phenomena that occur in space plasmas. To test this newly developed code, we performed simulations for both electrostatic and electromagnetic phenomena and compared the results with those of two widely used codes (Umeda 2004, Gary et al. 2011). For the test of the electrostatic phenomena, we applied the code to electron two-stream instabilities. For the

electromagnetic phenomena, whistler instabilities driven by electron temperature anisotropy were simulated.

In section 2, we briefly introduce the numerical schemes adopted in the code, and in section 3, we present test simulation results in comparison with those reported previously. Discussions and conclusions are presented in section 4.

2. METHOD

To handle various plasma processes we solve Maxwell's equations and relativistic Lorentz force equation as follows:

$$\frac{\partial \mathbf{E}}{\partial t} = -c^2 \mu_0 \mathbf{J} + c^2 \nabla \times \mathbf{B}, \quad (1)$$

$$\frac{\partial \mathbf{B}}{\partial t} = -\nabla \times \mathbf{E}, \quad (2)$$

© This is an Open Access article distributed under the terms of the Creative Commons Attribution Non-Commercial License (<http://creativecommons.org/licenses/by-nc/3.0/>) which permits unrestricted non-commercial use, distribution, and reproduction in any medium, provided the original work is properly cited.

Received Feb 26, 2015 Revised Mar 10, 2015 Accepted Mar 12, 2015

†Corresponding Author

E-mail: eslee@khu.or.kr, ORCID: 0000-0002-7737-0339
 Tel: +82-31-201-2047, Fax: +82-32-201-3852

$$\nabla \cdot \mathbf{E} = \frac{\rho}{\epsilon_0}, \tag{3}$$

$$\nabla \cdot \mathbf{B} = 0, \tag{4}$$

$$\frac{d}{dt}(\gamma_i \mathbf{v}_i) = \frac{q_i}{m_i}(\mathbf{E} + \mathbf{v}_i \times \mathbf{B}), \tag{5}$$

where E , B , J , and ρ are the electric field, magnetic field, current density, and charge density, respectively. In the Lorentz equation, q_i , m_i , v_i , and γ_i are the charge, rest mass, velocity, and Lorentz factor of the i -th particle, respectively. Maxwell's equations describe the variation of the electromagnetic fields, which affect the motion of charged particles according to the Lorentz force equation. Particles contribute to Maxwell's equations by the charge and current densities.

When particles are initially loaded into the simulation domain using a uniform random distribution, a small electric field can be produced by the non-uniformity of the charge density caused by the random distribution. Thus, we first solve the Poisson equation,

$$\nabla^2 \varphi = -\rho/\epsilon_0, \tag{6}$$

where φ is the electrostatic potential used to obtain the initial electric field. To solve the Poisson equation we use the successive over-relaxation (SOR) method (Press et al. 1992).

Next, we solve Faraday's induction equation, Eq. (2), using the leap-frog scheme to advance the magnetic field in time delineated by the following discretized equation.

$$\frac{\mathbf{B}^{n+1} - \mathbf{B}^n}{\Delta t} = -\nabla \times \mathbf{E}^{n+1/2} \tag{7}$$

Using the electric and magnetic fields we solve the relativistic Lorentz force equation, Eq. (5). As a result of using the leap-frog scheme, as in Eq. (7), the electric field and the magnetic field are determined at different times: the electric field at $(n + 1)\Delta t$, and the magnetic field at $(n + 1/2)\Delta t$. To obtain the values at the same time, $(n + 1)\Delta t$, we average the magnetic fields at $n\Delta t$ and $(n + 1)\Delta t$. To solve the relativistic Lorentz force equation we use the relativistic Buneman-Boris method (Birdsall & Langdon 2004).

Particles are then moved to new positions by solving the following equation:

$$\frac{d\mathbf{x}_i}{dt} = \mathbf{v}_i \tag{8}$$

Finally, we solve the Ampère-Maxwell equation, Eq. (1), using the current density and the magnetic field to advance the electric field in time. The estimation of the current density is complicated and many methods have been suggested to correctly calculate the current density (Villasenor & Buneman 1992, Esirkepov 2001, Umeda et al. 2003). Generally, we can calculate the current density as $\mathbf{J} = \sum_i n_i q_i \mathbf{v}_i$. However, this does not satisfy the charge conservation in discrete grid systems. To satisfy the charge conservation, we have to correct the electric field using some method, or the electric field must have a divergence-free part only. Alternatively, various methods have been suggested to satisfy the charge continuity equation as given below:

$$\frac{\partial \rho}{\partial t} + \nabla \cdot \mathbf{J} = 0. \tag{9}$$

Among the methods, we considered the Villasenor-Buneman method (Villasenor & Buneman 1992), the Esirkepov method (Esirkepov 2001), and the Zigzag method (Umeda et al. 2003). Each method has advantages and disadvantages. The Villasenor-Buneman method is the most accurate, but complex and time-consuming. The Esirkepov method exactly satisfies charge continuity, but makes small but broad linear-shape errors. The Zigzag method is the simplest approach, but makes high-value dot-like errors. Considering the respective advantages and disadvantages of the methods, we selected the Esirkepov method because of its simplicity and low-level errors. To diminish the errors of the method, we additionally smooth the current density by averaging the values at adjacent grids.

To solve the Poisson equation and calculate the current density it is necessary to estimate the charge density on the grids from particle distributions. The contribution of a particle to the charge density on a grid is determined by using shape functions. In this code, we use the second-order shape function in two-dimensions, given as follows:

$$S(x, y) = S(x)S(y) = \frac{1}{4}(1 - |x|)(1 - |y|). \tag{10}$$

Using the second-order shape function, one particle contributes to 9 adjacent grids. The higher-order shape function has the advantage of reducing numerical errors, but at the cost of large calculation time.

The time integration of all the differential equations is achieved by using the leap-frog scheme, as mentioned above. To carry out the leap-frog scheme, all the variables that have time dependence are divided into the variables

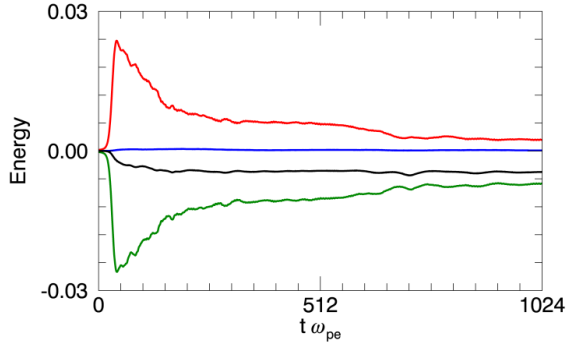


Fig. 1. Temporal variations of electric field energy density (red), magnetic field energy density (blue), kinetic energy density (green), and total energy density (black) averaged over the whole simulation domain. The values are normalized by $n_e m_e V_{te}^2$.

defined at the full-integer time step, $n\Delta t$, and those at the half-integer time step, $(n + 1)\Delta t$. For example, the magnetic field, current density, and velocity are defined at the full-integer time step while the electric field and position at the half-integer time step.

For the differentiation in space we use the centered difference scheme. In this scheme, the variables are defined either at a full-integer grid or at a half-integer grid, which is called a staggered grid system. For example, the charge density, electrostatic potential, and E_z are defined at the full-integer grid both in the x- and y-directions. On the other hand, E_x and B_y are defined at the half-integer grid in the x-direction and the full-integer grid in the y-direction, E_y and B_x are defined at the full-integer grid in the x-direction and the half-integer grid in the y-direction, and B_z is defined at the half-integer grid both in the x- and y-directions.

3. TEST OF THE DEVELOPED CODE

To test the developed code, we simulated the electron two-stream instability and the whistler instability using the same parameters as described in previously reported papers and compared the results with those of the previous papers.

3.1. Electron Two-Stream Instability

First, we simulated the electron two-stream instability with the parameters used by Umeda (2004). In this simulation, the length is normalized by the Debye length, λ_{De} , and time by the electron plasma frequency, ω_{pe} , satisfying $\lambda_{De} = v_{the} / \omega_{pe}$, where v_{the} is the electron thermal speed. The system size is $L_x \times L_y = 256\lambda_{De} \times 256\lambda_{De}$, and the number of grids is $N_x \times N_y = 256 \times 256$, which makes the grid size $\Delta x = \Delta y = 1.0\lambda_{De}$. The number of particles in a cell is set to be 128 for the electrons and protons, respectively. The ratio of the electron plasma frequency and the electron gyro-frequency

is set to be $\omega_{pe} / \Omega_{pe}$, and the electron thermal velocity $v_{the} = 0.05c$. The background magnetic field is oriented in the X-direction $B_0 = B_0 \hat{x}$, and the magnitude of the magnetic field, B_0 , is determined by the electron gyro-frequency. Boundary conditions are set to be periodic in both the X- and Y-directions.

To excite the electron two-stream instability, electron beams drifting oppositely to each other were initially injected uniformly throughout the simulation domain. The densities of the two beams were the same. The bulk speeds of the beams were $\pm 2v_{the}$, which makes the relative speed between the beams $4v_{the}$. To make the simulation conditions identical with Umeda (2004), we assumed that protons are immobile. This assumption is acceptable because the mass of protons is much larger than that of electrons and the electron two-stream instability develops in the time scale of electrons.

The simulation results are presented in Figs. 1 and 2. Fig. 1 shows the temporal variations of the electric field energy density, $\langle E^2 \rangle$, magnetic field energy density, $\langle B^2 \rangle$, kinetic energy density, $\langle nmv^2/2 \rangle$, and total energy density averaged over the whole simulation domain. Because the two-stream instability is an electrostatic instability, the electric field energy rapidly increases as the instability grows while the magnetic field energy remains almost constant. The increased electric field energy comes from the kinetic energy of particles, which decreases in coincidence with the increase of the electric field energy. This is consistent with the theory of the two-stream instabilities. After the electric field energy reached the maximum, it gradually decreased while the kinetic energy increased.

The drastic variations of energies in the growth phase of the instability produced numerical errors, which caused a loss of the total energy. However, during gradual variations of energies, the total energy was well conserved. In comparison with the results of Umeda (2004), the variations of the energies are similar except for that in the case of Umeda (2004) the total energy density gradually decreased even after the decrease in the rapid growth phase.

Fig. 2 shows the distribution of the electrostatic potential at $\omega_{pe} t = 60$, $\omega_{pe} t = 260$, and $\omega_{pe} t = 1020$. Because the two electron beams drift oppositely along the background magnetic field, the electrostatic waves propagate parallel to B_0 producing sinusoidal oscillations of the potential (Fig. 2a), which are represented as electron holes in the phase space. After the instability reached saturation at $\omega_{pe} t \sim 60$, the wave structures or electron holes merged together until there remained only one structure. In comparison with the results of Umeda (2004), the wave structures are very similar in the early development stage in Fig. 2a. In Figs. 2b and 2c,

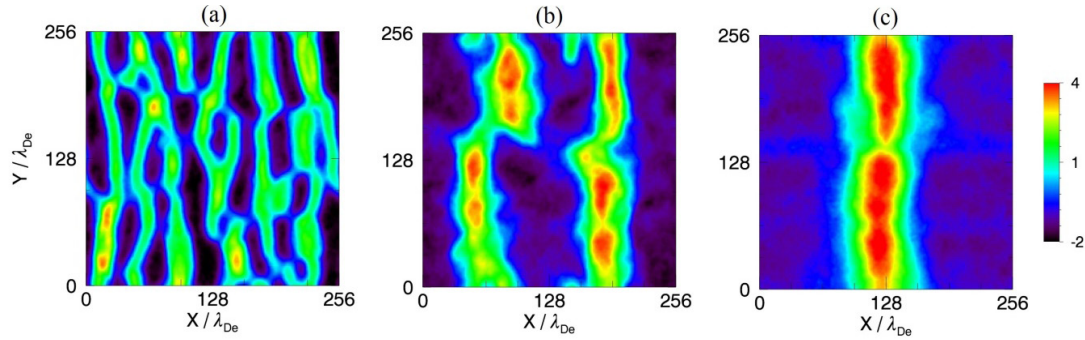


Fig. 2. Distribution of electrostatic potential at (a) $w_{pe}t = 60$, (b) $w_{pe}t = 260$, and (c) $w_{pe}t = 1020$.

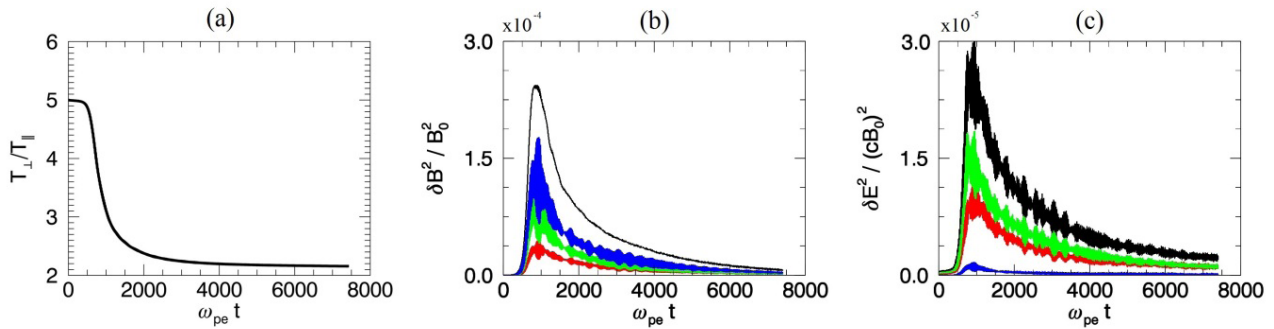


Fig. 3. Temporal variations of (a) temperature anisotropy, (b) magnetic energy density, and (c) electric energy density. Red, green, blue, and black colors in (b) and (c) represents the x-, y-, z-components and the magnitude, respectively.

however, the merging of the structures was slightly faster in our results than in Umeda (2004), which might be related to the difference in the variations of the energies.

3.2. Electron Temperature-driven Whistler Instability

Next, we followed the initial configurations of Run 3 in Gary et al. (2011), who investigated the electron temperature-driven whistler instability using their PIC code. The simulation system is normalized by λ_e in space and w_{pe} in time, satisfying $\lambda_e = c / w_{pe}$, where λ_e is the electron inertial length. The system size is $L_x \times L_y = 12.85\lambda_e \times 12.85\lambda_e$, the number of grids is $N_x \times N_y = 64 \times 64$, and the number of particles is set to be 9600 particles in a cell for each of the electrons and protons. The ratio of electron plasma frequency and electron gyro-frequency is set to be $w_{pe} / \Omega_{ce} = 4.0$, where $\Omega_{ce} = eB / m_e$ is the electron gyro-frequency. Ions are assumed to be an immobile background as in the previous case. Periodic boundary conditions are used for both the x- and y-directions. The background magnetic field is applied along the x-direction, $B_0 = B_0 \hat{x}$.

To excite the instability, the electron temperature anisotropy in the perpendicular and parallel directions to the background magnetic field is applied as $T_{\perp e} / T_{\parallel e}$, and

the parallel plasma beta of electrons is given as $\beta_{\parallel e} = 0.01$.

Fig. 3 shows the temporal variations of the temperature anisotropy, $T_{\perp e} / T_{\parallel e}$, magnetic energy density, $\delta B^2 / B_0^2$, and electric energy density, $\delta E^2 / (cB_0)^2$, of the fluctuations. As the instability grew, the temperature anisotropy decreased rapidly while the electric and magnetic energy densities increased. The kinetic energy density decreased in coincidence with the increase of electric and magnetic energy densities (not shown). Note that the magnetic energy density is an order of magnitude larger than the electric energy density. The growth of the B_z component was dominant, which corresponds to the growth of the E_x and E_y components. In comparison with the results of Gary et al. (2011), all the variations are almost the same except for that our results evolve slightly faster. It should be noted that time was normalized by the electron cyclotron frequency in Gary et al. (2011), but in our simulation it was normalized by the electron plasma frequency. The ratio between the frequencies is $\omega_{pe} / |\Omega_e| = 4$, where ω_{pe} and Ω_e are the electron plasma frequency and the cyclotron frequency, respectively.

Fig. 4 shows the distributions of $B_z(x, y)$ in the configuration space and $B_z(k_{\parallel}, k_{\perp})$ in the k-space at $\omega_{pe}t = 740$ when the instability is close to saturation. It is seen that the

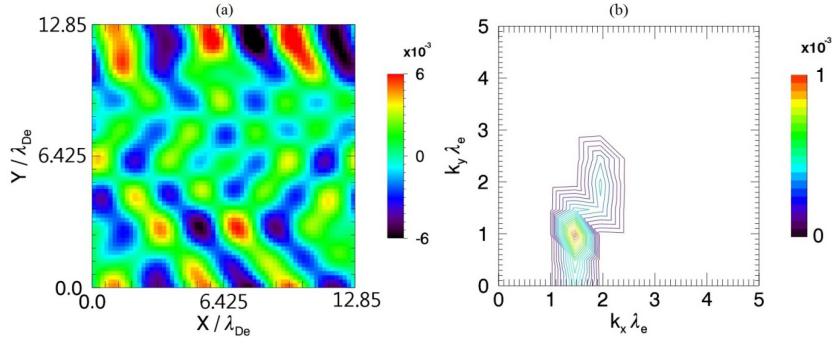


Fig. 4. (a) Spatial distribution of B_z and (b) the corresponding spectrum in k -space at $w_{pe}t = 720$.

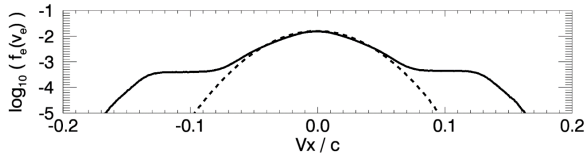


Fig. 5. Velocity distribution of electrons in the direction parallel to the background magnetic field. The dashed line shows the initial velocity distribution and the solid line the distribution at $w_{pe}t = 7400$ ($\Omega_e t = 1850$).

whistler waves propagate obliquely. The spatial distribution of the B_z component and the propagation characteristics of the whistler waves in our simulation results are almost identical with those of Gary et al. (2011). The only difference is that the wave number, k , of our results is slightly smaller than that of Gary et al. (2011), which implies that the wavelength of the generated whistler waves is slightly longer in our results.

Fig. 5 shows the parallel velocity distribution of electrons at the initial and final stages of the simulation. As a result of the instability, suprathermal electrons were generated in the range of $4 \leq |v_{\parallel e}|/v_{the} \leq 6$ in the direction parallel to the background magnetic field. The generation of suprathermal electrons in the parallel direction reduced the temperature anisotropy, $T_{\perp e}/T_{\parallel e}$. However, it should be noted that the temperature is not well defined for the distribution seen in Fig. 5 because the distribution is a non-Maxwellian distribution consisting of the core and suprathermal components. According to Gary et al. (2011), the suprathermal electrons were produced by the acceleration by the parallel component of the electric field through Landau resonance. The velocity distribution of electrons is also consistent with that of Gary et al. (2011).

4. DISCUSSION AND CONCLUSION

In this paper, we briefly introduced the 2.5-dimensional relativistic electromagnetic PIC code that we have

developed and tested the performance of the code by comparing the results obtained from the code with those of two widely used codes reported in previous studies.

First, we performed a simulation of the electron two-stream instability to test the availability of handling the plasma dynamics in electrostatic phenomena. Our simulation results captured most of the physical features presented in Umeda (2004) except that merging of the electron holes in the relaxation phase took place slightly faster in our simulation. Note that both codes suffered similar numerical errors during the rapid growth of the instability. The loss of the total energy appears to be related with numerical diffusion and our code has slightly larger numerical diffusion than Umeda's. This also appears in the merging rate of the electron holes, which is faster in our results than those of Umeda. Thus, we should be cautious for unphysical loss or gain of energies when a process occurs rapidly. However, the loss or gain of energies was not significant enough to affect the main physical processes.

Next, we performed a simulation of the whistler instability driven by electron temperature anisotropy to test for handling the plasma dynamics in electromagnetic phenomena. In this case, our simulation successfully produced the whistler instability and the results of our simulation were also almost identical with those of Gary et al. (2011). A slight difference was found in the wavelength of the generated whistler waves. However, this did not substantially affect the main features of the instability.

In conclusion, the PIC code we have developed successfully reproduced most of the physical features reported in previous studies for both electrostatic and electromagnetic phenomena. We will further improve the code in future studies to reduce the numerical errors by applying higher-order shape functions or by implementing other numerical schemes.

ACKNOWLEDGEMENTS

This work was in part supported by the Basic Science Research Program (NRF-2013R1A1A2010711) and the BK21 Plus Program through the National Research Foundation (NRF) funded by the Ministry of Education of Korea, and the grant CATER2012-5060 from the Center for Atmospheric Science and Earthquake Research in Korea.

REFERENCES

- Birdsall CK, Langdon AB, Plasma Physics via Computer Simulation (CRC Press, New York, 2004).
- Esirkepov TZ, Exact Charge Conservation Scheme for Particle-In-Cell Simulation with an Arbitrary Form-factor, Comput. Phys. Comm. 135, 144-153 (2001). [http://dx.doi.org/10.1016/S0010-4655\(00\)00228-9](http://dx.doi.org/10.1016/S0010-4655(00)00228-9)
- Gary SP, Liu K, Winske D, Whistler anisotropy instability at low electron β : Particle-in-cell simulations, Phys. Plasma. 18, 082902 (2011). <http://dx.doi.org/10.1063/1.3610378>
- Press WH, Teukolsky SA, Vetterling WT, Flannery BP, Numerical Recipes in Fortran 77 (Cambridge University Press, New York, 1992).
- Umeda T, Omura Y, Tominaga T, Matsumoto H, A new charge conservation method in electromagnetic particle-in-cell simulations, Comput. Phys. Comm. 156, 73-85 (2003). [http://dx.doi.org/10.1016/S0010-4655\(03\)00437-5](http://dx.doi.org/10.1016/S0010-4655(03)00437-5)
- Umeda T, Study on Nonlinear Processes of Electron Beam Instabilities via Computer Simulations, PhD Dissertation, Kyoto University (2004).
- Villasenor J, Buneman O, Rigorous charge conservation for local electromagnetic field solvers, Comput. Phys. Comm. 69, 306-316 (1992). [http://dx.doi.org/10.1016/0010-4655\(92\)90169-Y](http://dx.doi.org/10.1016/0010-4655(92)90169-Y)